Microspectroscopic two-dimensional Fermi surface mapping using a photoelectron emission microscope

M. Kotsugi,[a] W. Kuch, F. Offi, L. I. Chelaru, and J. Kirschner
Max-Planck-Institut für Mikrostrukturphysik, Weinberg 2, D-06120 Halle, Germany

(Received 25 October 2002; accepted 20 December 2002)

We demonstrate the use of a photoelectron emission microscope in connection with a retarding field electron energy analyzer for the fast acquisition of two-dimensional momentum resolved photoelectron angular distribution patterns. This opens the possibility to combine spatial, momentum, and energy resolution of photoelectrons within the same instrument. We have applied this to observe the Cu(001) Fermi surface from a selected region of the sample. A well defined bulk Fermi surface is quickly mapped in this way. © *2003 American Institute of Physics.*
[DOI: 10.1063/1.1569404]

I. INTRODUCTION

Numerous techniques that rely on the detection of photoemitted electrons have been successfully used in the past years for the investigation of surfaces and thin films. Detection of photoexcited electrons has been used in both microscopic and spectroscopic approaches.[1–23] In the former, the spatial intensity distribution of photoelectrons is microscopically imaged in real space, often without energy analysis. A prominent example is photoelectron emission microscopy (PEEM).[1–9] The latter, spectroscopic techniques, usually involve electron momentum and energy resolution, as in angle resolved photoelectron spectroscopy (ARPES), a powerful technique for the study of electronic properties.[12–22] Only a few attempts have been made so far on photoelectron energy spectroscopy with simultaneous spatial and momentum resolution.[23]

In this article, we demonstrate that photoelectron energy and momentum resolution can be achieved by using a PEEM in connection with a simple retarding field imaging energy analyzer. The common usage of PEEM is to obtain spatially resolved microscopic images of the sample surface.[1–7] It is, however, also possible in a PEEM to obtain electron momentum resolution of the component parallel to the surface by changing the projection electron lens optics settings to display the focal plane instead of the image plane. If the transmitted electrons are energy filtered, the projected image in this mode represents the photoelectron angular distribution pattern. In addition, since a microscope is used, the photoelectrons contributing to this pattern can be spatially selected in real space by using a field aperture, in order to detect only photoelectrons from a small area of the sample. This can be a great advantage for the study of electronic properties of inhomogeneous samples, for example micropatterned samples.

The simplest way for energy filtering of electron images is to pass the two-dimensional electron distribution through a retarding grid. While this has, in general, the disadvantage that only high-pass filtering is achieved, and two images need to be subtracted to obtain a band-pass filtered image, it can be conveniently used to obtain band-pass filtered images without subtraction at the Fermi energy, where the Fermi distribution function of the sample provides the corresponding low-pass cutoff. Photoelectron spectroscopy mapping of Fermi surfaces has contributed significant knowledge about the electronic structure of solids.[15–22] We show the feasibility of using an energy-filtered PEEM for Fermi surface mapping by applying the method to the imaging of the Fermi surface of a Cu(001) single crystal. Two-dimensional photoelectron angular distribution patterns could be quickly acquired with an energy resolution better than 0.62 eV and momentum resolution better than 0.2 $Å^{-1}$. A three-dimensional scan of the bulk Cu Fermi surface by varying the photon energy of the exciting synchrotron radiation could be performed in less than 1/2 h.

II. EXPERIMENT

All experiments presented here were performed at the undulator beamline UE56/2 PGM-2 of the synchrotron radiation facility BESSY II in Berlin.[24] Linearly *s*-polarized radiation of the first harmonics of the undulator was used for the excitation, incident to the sample under an angle of 60° from the surface normal in the [010] crystallographic azimuth of the Cu(001) single crystal. The photon energy resolution was about 0.15 eV for the photon energies used here, which were around 100 eV. We used a commercially available PEEM (Focus IS-PEEM), in which an imaging energy filter was inserted between the drift tube and the image detection unit. A schematic setup of the instrument is shown in Fig. 1. The microscope consists of the three-element objective lens, which creates an intermediate real space image of the emitted electron intensity distribution of the sample in the image plane. A high electric field (typically 10–15 kV) is applied between the sample and the first element of the objective lens to accelerate the emitted photoelectrons. As a convenient side effect, electrons from a larger solid angle contribute to the image, thus widening the maximum acceptance angle. The contrast aperture, located in the back focal plane

[a]Author to whom correspondence should be addressed; electronic mail: kotsugi@mpi-halle.de

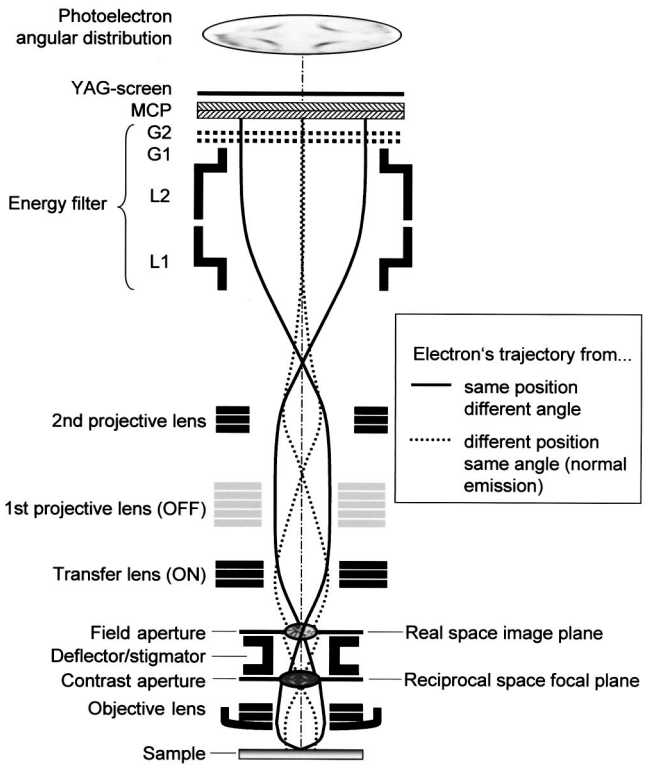

FIG. 1. Schematic view of the lens optics of the PEEM. The objective lens creates an image of the photoelectron angular distribution of the sample surface in the focal plane, and an image of the spatial photoelectron intensity distribution in the image plane. In the momentum resolving mode, transfer lens and projective lenses are set to project the photoelectron angular distribution of the reciprocal space focal plane onto the multichannel plate. Shown are also photoelectron trajectories for electrons emitted from the same position under different emission angles (solid lines), and for electrons emitted from different positions under the same angle (dotted line). A continuously size-variable field aperture located in the image plane can be used as sample microspot selector.

of the objective lens, was set to its maximum size of 1200 μm diameter in order to allow the largest possible range of electron parallel momentum to be transmitted. An electrostatic octupole stigmator/deflector can be used for the correction of astigmatism and the alignment of the optical axis in any rotational direction. A set of electrostatic lenses, consisting of the transfer lens, two projective lenses, and two lenses of the imaging energy filter (*L1* and *L2*) can be set to project either the real space photoelectron distribution of the image plane or the angular distribution pattern of the focal plane onto the double multichannel plate (MCP). We call these two modes the ''microscopic mode'' and the ''momentum resolving mode.'' Schematic electron trajectories shown in Fig. 1 represent the latter mode of operation, in which the first projective lens is switched off, while the transfer lens is on. Displayed are two selected sets of electron trajectories, emitted from the same position of the sample under different angles (continuous lines), and emitted from different positions under the same angle (normal to the sample surface, dotted lines). For the measurements presented here, the objective lens was operated at 10 kV extraction voltage, and the projection optics was set to give a field of view of about ± 2.4 Å^{-1} in the momentum resolving mode. That easily covers the first and a part of the second surface Brillouin zone of Cu(001).

A continuously size variable hexagonal field aperture located in the image plane can be used to select a microscopic region of the sample from which photoelectrons are accepted. This region is usually selected using the imaging mode, following the limiting effect of the field aperture by looking at the live image of the sample surface. This ''microspot selector'' allows one to select well defined sample areas of down to about 1 μm diameter, since all of the lenses between the sample and the field aperture are kept at identical voltages in both modes to maintain the same spatially resolved region of interest. For the measurements presented here, it was set to detect electrons from an area of approximately 130 μm diameter.

For the energy analysis of the electrons, the instrument was equipped with an imaging energy filter[4,25] consisting of two additional cylindrical lenses *L1* and *L2*, and two grids *G1* and *G2*. The two lens elements *L1* and *L2* form the preretardation optics, and are set to decelerate the electrons and to reach normal incidence on the subsequent grids. The two grids *G1* and *G2* form the homogeneous electric field that acts as the high-pass energy filter. The first grid *G1* is mechanically and electrically connected to *L2*. The second grid *G2* is the retarding grid at voltage U_G, which allows only transmission of electrons with a kinetic energy higher than eU_G. Thus, this imaging energy filter unit acts as a retarding field analyzer. All electrons with a true starting energy $E_0 > eU_{\text{sample}} - eU_G$, where U_{sample} is the sample voltage, can pass the second grid *G2* and reach the imaging unit. For the present measurements, *L1* and *L2* were set to $+250$ V and $+94$ V, respectively. *G2* was kept at a constant voltage of $+50$ V, whereas the sample voltage was varied to select high-pass energy filtering at energy $E_0 = e(U_{\text{sample}} - 50\ \text{V})$.

The magnified image is intensified by the double MCP, and converted into visible light by means of a scintillator (YAG) crystal. The image is then computer recorded with 12-bit resolution by a Peltier cooled camera (PCO SensiCam). A 4×4 binning of camera pixels was used for the images presented here. To reduce the amount of data, the region of interest was limited to a square of 128×128 image pixels, covering the complete angular distribution pattern. The experiment was performed at room temperature in an ultrahigh vacuum chamber with a base pressure of 2×10^{-8} Pa in the sample preparation chamber, and 4×10^{-8} Pa in the measurement chamber.

The Cu(001) single crystal used for the experiments was cleaned by Ar^+ ion sputtering of 1.5 keV energy, and subsequent short annealing up to approximately 820 K. After this treatment, the sample surface cleanliness was checked by Auger electron spectroscopy, and the surface order was checked by low-energy electron diffraction.

III. RESULTS AND DISCUSSION

The energy resolution of the imaging energy filter with the instrument settings described in Sec. II was evaluated from work function threshold photoemission. This experiment was performed on a 15 ML thick Fe film deposited at room temperature on Cu(001). A series of images was acquired by scanning the sample voltage through the work

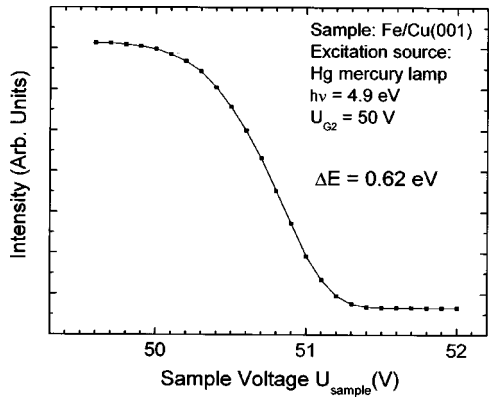

FIG. 2. Work function threshold of the imaging energy filter, showing the integrated image intensity (symbols) of a 15 ML thick Fe film on Cu(001) as a function of sample voltage for excitation with an Hg lamp (4.9 eV photon energy). The energy resolution is estimated as 0.62 eV by a fit with a Gaussian step function (solid line).

function threshold. An Hg lamp was used as an excitation source with a photon energy of 4.9 eV. The sample voltage U_{sample} was scanned from +49.5 to +52.0 V in 0.1 V steps with a fixed retarding grid voltage, U_G, of +50 V, corresponding to a scan around zero electron energy. At each voltage step, the integrated image intensity from a 10 s exposure was recorded. It is plotted as a function of sample voltage in Fig. 2 (symbols). An upper bound for the energy resolution is estimated by fitting a Gaussian step function to the resulting electron energy distribution curve (solid line in Fig. 2), which yields a Gaussian full width at half maximum (FWHM) of 0.62 eV.

In order to estimate the angular acceptance, one has to consider the lens optics and the kinetic energy of the electrons. A particularity of using an immersion lens microscope is that the angular distribution images are scaled to the parallel component of the momentum rather than to the emission angle. This is because the emission angle α' "seen" by the instrument, i.e., the incident angle to the objective lens after the electron has been accelerated by the extractor voltage, and the true starting angle α_0 at the sample surface are related by

$$\sin\alpha_0 = \sin\alpha' \sqrt{\frac{eU_{\text{ex}}}{E_0}+1}, \tag{1}$$

where E_0 is the true starting kinetic energy of the photoelectrons, and U_{ex} is the accelerating voltage between sample and objective lens.[26] This is because the extraction high-voltage changes only the component of the photoelectron momentum perpendicular to the surface, $k_\perp$, while the component parallel to the surface $k_\parallel$ is not changed because of cylinder symmetry. The maximum value of α' depends on the geometry of the instrument, and is about 2.4° in the present case. The maximum acceptance angle at $E_0 = 90$ eV is thus $\alpha_0 = \pm 26°$. The emission angle α_0 depends on $k_\parallel$ and the total momentum k as $\sin\alpha_0 = k_\parallel/k$. Since $k \propto \sqrt{E_0}$, it follows from Eq. (1) that $\sin\alpha' \propto k_\parallel$, provided $E_0 \ll U_{\text{ext}}$. This means that for a fixed $k_\parallel$, the angle α' seen by the instrument is always the same, in contrast to the real emission angle α_0, which changes with varying energy. This fixed

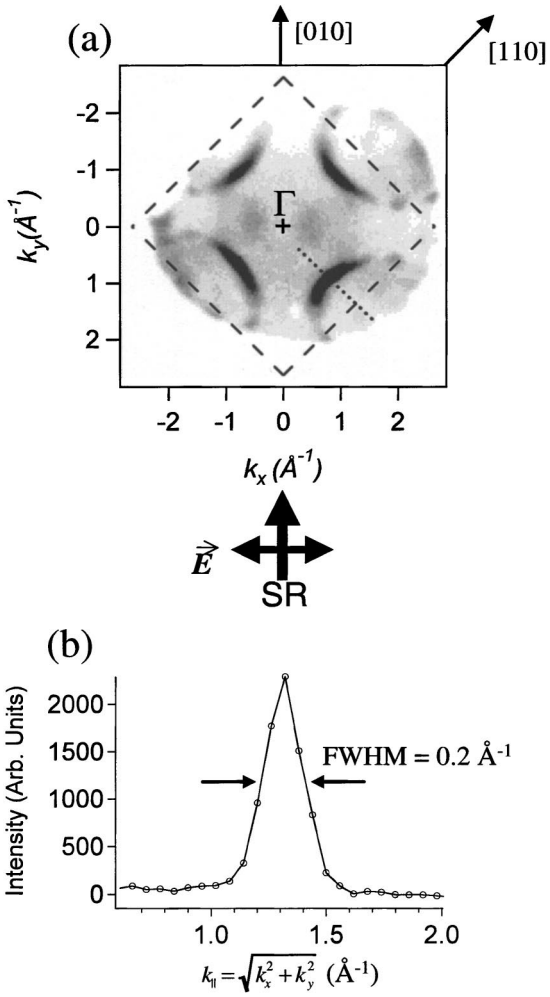

FIG. 3. (a) Spot-selected two-dimensional photoelectron angular distribution pattern for photoemission from the Fermi energy of Cu(001) for 95 eV photon energy from an area of 130 μ m diameter on the surface. The dashed line indicates the surface Brillouin zone of Cu(001). The synchrotron radiation incidence direction is indicated by an arrow "SR," and the direction of its *s*-polarized electric vector is indicated by an arrow "*E*." (b) Intensity line profile from the dotted line of (a). The FWHM is estimated as 0.2 Å^{-1} in momentum space, which corresponds to 2.2° in the angular scale at the given energy.

scale of the images with respect to $k_\parallel$ facilitates the analysis of photoelectron angular distribution patterns taken at different electron energies. The position on the screen can thus be calibrated directly in the units of $k_\parallel$. For the settings used here, 23.6 image pixels corresponded to 1 Å^{-1}.

Figure 3(a) shows a spot-selected two-dimensional photoelectron angular distribution pattern of Cu(001), recorded at the Fermi energy. The photon energy was 95 eV, and the sample voltage was 139.5 V in order to detect photoelectrons only from near the Fermi level. A background image taken at 1.5 V higher retarding voltage (141 V) was subtracted. Both images were exposed 10 s with 16 times average, thus the total exposure time was 320 s. The resulting photoelectron intensity distribution is represented on a grayscale as a function of the two components of the electron momentum parallel to the surface, k_x and k_y.

The shape of the well-known Cu Fermi surface is clearly reproduced. The dashed line in Fig. 3(a) indicates the surface

Brillouin zone. The circle segments observed in each corner of the surface Brillouin zone correspond to a slice of the surrounding Fermi surfaces in the second Brillouin zone, whereas the weaker intensity in the center corresponds to a slice of the Fermi surface of the first Brillouin zone. The two-fold shape of the latter is due to the linear light polarization,[27–29] the electric vector of which is indicated as an arrow in Fig. 3. The acquisition time of such a two-dimensional Fermi surface map is quite short compared to usual ARPES.

An upper bound for the momentum resolution can be evaluated from the width of the features of this Fermi surface image. Figure 3(b) shows a line scan along the white dotted line of Fig. 3(a). The corresponding line profile of the photoelectron intensity is shown in Fig. 3(b) as a function of $k_{\parallel}$. The FWHM is estimated as 0.2 Å^{-1} in momentum space, which corresponds to 2.3° at this kinetic energy.

The fast acquisition time of the two-dimensional photoelectron distribution patterns allows a complete three-dimensional Fermi surface mapping. This is done in the so-called constant initial state mode. In this mode, both photon energy and high-pass filtering energy are scanned simultaneously. The difference between photon energy and sample voltage is kept fixed to detect only electrons emitted from the Fermi edge. Thus, the initial state energy of the photoelectrons is constant, while the final state energy is scanned. This electron energy scanning corresponds to scanning $k_{\perp}$ in momentum space, which is proportional to the square root of the electron energy assuming free-electronlike final states.

We have taken 59 images by scanning the sample voltage U_{sample} from 111.5 V to 169.5 V in steps of 1 V, while the photon energy was simultaneously scanned from 67 eV to 125 eV with the same steps. This corresponds to scanning E_0 from 61.5 eV to 119.5 eV. The binding energy was thus the same as in Fig. 3(a), close to zero with respect to the Fermi energy. A background image was obtained at 1.5 eV above each signal image, thus from 113 to 171 V sample voltage. The exposure time for one image was only 20 s.

The resulting images change gradually and continuously with energy. Figures 4(a)–4(d) show Fermi surface images at four selected photon energies, indicated at each image. The two vertical stripelike features seen in Fig. 4(a) approach each other and subsequently nearly disappear as $\hbar\omega$ is increased [Fig. 4(b)], before they reappear and again become more separated upon further increasing the photon energy [Figs. 4(c) and 4(d)]. This comes from crossing from the Cu Fermi surface of the second to the Fermi surface of the third Brillouin zone close to the X point. Figure 4(e) shows a schematic cut through the Cu Fermi surface along the (100) plane. Solid lines indicate the Cu Brillouin zone, whereas dashed lines reproduce the Cu Fermi surface. As is well known, the Cu Fermi surface is face-centered-cubic shaped with eight necks and octahedral connections to neighboring Fermi surfaces. The dotted circle segments show where each of the images Figs. 4(a)–4(d) and Fig. 3(a) cuts through this plane, assuming free-electronlike final states. In this approximation, $k_{\perp}$ can be estimated from the electron energy E_0 and the in-plane component of the electron momentum $k_{\parallel}$ as

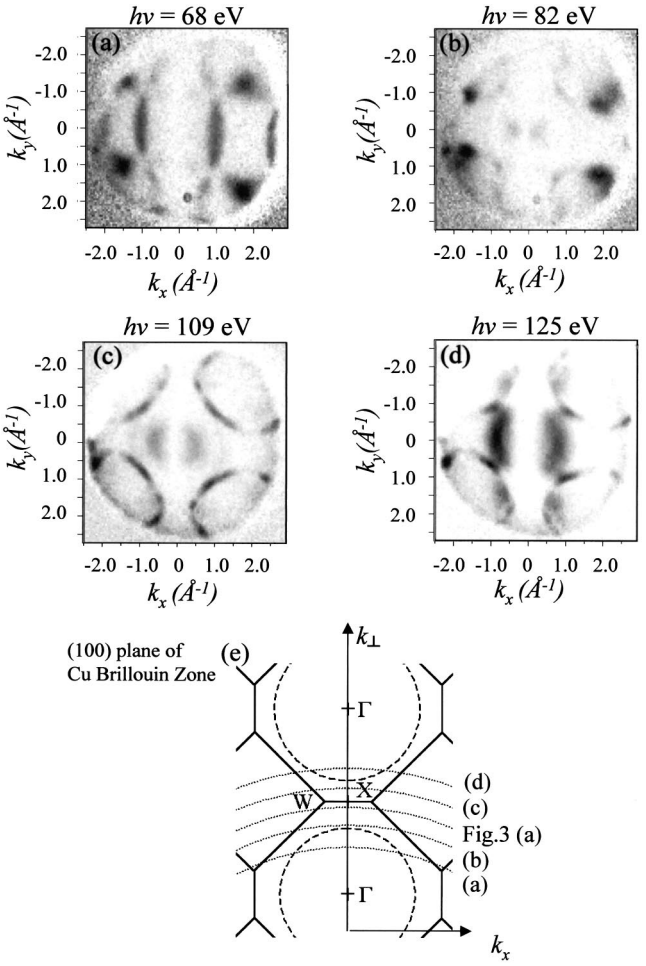

FIG. 4. (a)–(d) Selected images from a constant initial energy scan of a stack of 59 images of the Fermi energy photoelectron angular distribution patterns of Cu(001). (e) Schematic diagram showing a cut through the (100) plane of the Brillouin zone. The Cu Fermi surface is indicated by solid lines. Dashed lines mark the Brillouin zone boundaries. The corresponding slice of each image presented in (a)–(d) as well as in Fig. 3(a) is given by dotted lines assuming free electrons for the final states.

$$k_{\perp} = \sqrt{\frac{2m}{\hbar^2}(E_0 + V_0) - k_{\parallel}^2}, \tag{2}$$

where m is the electron mass, $\hbar$ is the Planck constant, and V_0 is the inner potential, which was taken as 13.5 eV.[30] $k_{\parallel}$ is directly extracted from the pixel position on the image, as discussed herein. The complete energy scan range corresponds thus to a scan from $k_{\perp}=4.4$ to 5.9 Å^{-1} at $k_{\parallel}=0$. In the images, the (100) plane intersects at a horizontal line at $k_y=0$. It can be seen how upon increasing $k_{\perp}$, the Fermi surface is probed across the X point, which leads to the observed behavior of the central two features.

From the three-dimensional stack of data, the three-dimensional Cu Fermi surface of a spot-selected region can be obtained. To do so, the data were converted into a three-dimensional set of intensity values for k_x, k_y, and $k_{\perp}$ using Eq. (2). Figure 5 presents a cut through this data set along the (110) plane. The Brillouin zone is indicated as a solid line. The crystallographic points X, U, and L are also shown in Fig. 5. The typical ''dog bone''-shaped Fermi surface is displayed by dashed lines in Fig. 5. In the images, the (110)

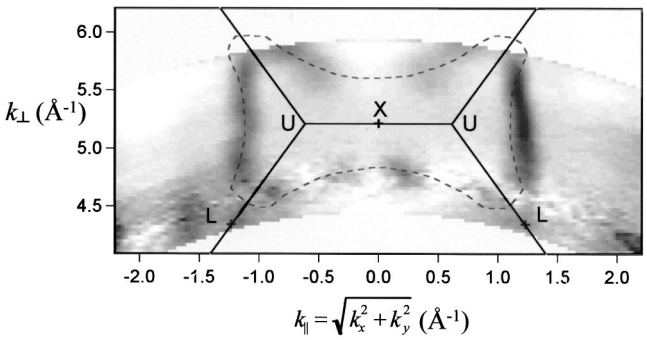

FIG. 5. Slice along the (110) plane from the three-dimensional data set of Cu(001) of Fig. 4. The Cu Fermi surface is indicated by solid lines. Dashed lines mark the Brillouin zone boundaries. The typical dog bone-shaped Fermi surface is observed.

plane intersects at a diagonal line with $k_x = k_y$. It is clearly seen that the experimental intensity closely follows the Fermi surface. At higher $k_\parallel$ around ± 1.2 Å^{-1}, the shape of the dog bone is nicely reproduced. The missing intensity observed near $k_\parallel = 0$ is due to the use of *s*-polarized light for the same reason as discussed in connection with Fig. 3, and does therefore not correspond directly to the density of states.

These data show that simultaneous energy, momentum, and spatial resolving photoelectron spectroscopy is possible using a PEEM. The use of a PEEM with a simple imaging retarding grid electron energy analyzer is especially well suited for studies of photoemission from the Fermi edge. The relatively high intensity allows short exposure times, and the rapid acquisition of three-dimensional data stacks becomes possible. Advantages of this method are the quick acquisition, and the possibility to obtain microspectroscopic information. As an alternative to dedicated two-dimensional electron analyzers, PEEM plus energy filtering promises a high potential for the investigation of the electronic structure of laterally inhomogeneous samples or small samples.

ACKNOWLEDGMENTS

The authors would like to thank B. Zada and W. Mahler for their expert technical support. Financial support by the German Federal Minister for Education and Research (BMBF) under Grant No. 05KS1EFA6 is gratefully acknowledged.

[1] W. Kuch, X. Gao, and J. Kirschner, Phys. Rev. B **65**, 064406 (2002).
[2] W. Kuch, R. Frömter, J. Gilles, D. Hartmann, C. Ziethen, C. M. Schneider, G. Schönhense, W. Swiech, and J. Kirschner, Surf. Rev. Lett. **5**, 1241 (1998).
[3] W. Kuch, J. Gilles, F. Offi, S. S. Kang, S. Imada, S. Suga, and J. Kirschner, Surf. Sci. **480**, 153 (2001).
[4] M. Merkel, M. Escher, J. Settemeyer, D. Funnemann, A. Oelsner, C. Ziethen, O. Schmidt, M. Klais, and G. Schönhense, Surf. Sci. **480**, 196 (2001).
[5] Y. Hwu, W. L. Tsai, B. Lai, J. H. Je, G. H. Fecher, M. Bertolo, and G. Margaritondo, Surf. Sci. **480**, 188 (2001).
[6] J. Stöhr, Y. Wu, B. D. Hermsmeier, M. G. Samant, G. R. Harp, S. Koranda, D. Dunham, and B. P. Tonner, Science **259**, 658 (1993).
[7] S. Anders, H. A. Padmore, R. M. Duarte, T. Renner, T. Stammler, and A. Scholl, Rev. Sci. Instrum. **70**, 3973 (1999).
[8] W. Swiech, G. H. Fecher, C. Ziethen, O. Schmidt, G. Schönhense, K. Grzelakowski, C. M. Schneider, R. Frömter, H. P. Oepen, and J. Kirschner, J. Electron Spectrosc. Relat. Phenom. **84**, 171 (1997).
[9] C. M. Schneider, J. Magn. Magn. Mater. **175**, 160 (1997).
[10] F. J. A. den Broeder, W. Hoving, and P. J. H. Bloemen, J. Magn. Magn. Mater. **93**, 562 (1991).
[11] J. Bansmann, M. Getzlaff, G. Schönhense, M. Fluchtmann, and J. Braun, Surf. Sci. **402–404**, 365 (1998).
[12] K. Rossnagel, L. Kipp, M. Skibowski, C. Solterbeck, T. Strasser, W. Schattke, D. Voß, P. Krüger, A. Mazur, and J. Pollmann, Phys. Rev. B **63**, 125104 (2001).
[13] H. Nishimoto, H. Daimon, S. Suga, S. Imada, T. Matsushita, T. Nakatani, H. Namba, T. Ohta, Y. Kagoshima, and T. Miyahara, J. Electron Spectrosc. Relat. Phenom. **78**, 465 (1996).
[14] R. H. Gaylord, K. H. Joeng, and S. D. Kevan, Phys. Rev. Lett. **62**, 2036 (1989).
[15] P. Aebi, J. Osterwalder, R. Fasel, D. Naumovic, and L. Schlappbach, Surf. Sci. **307–309**, 917 (1994).
[16] P. Aebi, T. J. Kreutz, J. Osterwalder, R. Fasel, P. Schwaller, and L. Schlappbach, Phys. Rev. Lett. **76**, 1150 (1996).
[17] G. J. Mankey, K. Subramanian, R. L. Stockbauer, and R. L. Kurtz, Phys. Rev. Lett. **78**, 1146 (1997).
[18] T. Greber, T. J. Kreutz, and J. Osterwalder, Phys. Rev. Lett. **79**, 4465 (1997).
[19] T. Straub, R. Claessen, P. Steiner, S. Hüfner, V. Eyert, K. Friemelt, and E. Bucher, Phys. Rev. B **55**, 13473 (1997).
[20] M. Hochstrasser, N. Gilman, R. F. Willis, F. O. Schumann, J. G. Tobin, and E. Rotenberg, Phys. Rev. B **60**, 17030 (1999).
[21] J. Schäfer, E. Rotenberg, G. Meigs, S. D. Kevan, P. Blaha, and S. Hüfner, Phys. Rev. Lett. **83**, 2069 (1999).
[22] F. Baumberger, T. Greber, and J. Osterwalder, Phys. Rev. B **64**, 195411 (2001).
[23] Th. Schmidt, S. Heun, J. Slezak, J. Diaz, K. C. Prince, G. Lilienkamp, and E. Bauer, Surf. Rev. Lett. **5**, 1287 (1998); E. Bauer, J. Electron. Spectrosc. Relat. Phenom. **114–116**, 975 (2001).
[24] M. R. Weiss *et al.*, Nucl. Instrum. Methods Phys. Res. A **467–468**, 449 (2001).
[25] Focus Imaging Energy Filter (Omicron).
[26] G. Schönhense, J. Phys.: Condens. Matter **11**, 9517 (1999).
[27] J. B. Pendry, *Low Energy Electron Diffraction* (Academic, London, 1974), p. 23.
[28] A. B. Pippard, *Dynamic of Conduction Electrons* (Gordon and Breach, New York, 1965).
[29] J. M. MacLaren, S. Crampin, D. D. Vvedensky, R. C. Albers, and J. B. Pendry, Comput. Phys. Commun. **60**, 365 (1990).
[30] S. M. Goldberg, C. S. Fadley, and S. Kono, J. Electron Spectrosc. Relat. Phenom. **21**, 285 (1981).